Theoretical model for optical oximetry at the capillary level: exploring hemoglobin oxygen saturation through backscattering of single red blood cells

Rongrong Liu
Graham Spicer
Siyu Chen
Hao F. Zhang
Ji Yi
Vadim Backman

SPIE.

Theoretical model for optical oximetry at the capillary level: exploring hemoglobin oxygen saturation through backscattering of single red blood cells

Rongrong Liu,[a] Graham Spicer,[b] Siyu Chen,[a] Hao F. Zhang,[a,c] Ji Yi,[d,*] and Vadim Backman[a,*]
[a]Northwestern University, Department of Biomedical Engineering, Evanston, Illinois, United States
[b]Northwestern University, Department of Chemical and Biological Engineering, Evanston, Illinois, United States
[c]Northwestern University, Department of Ophthalmology, Chicago, Illinois, United States
[d]Boston University, Department of Medicine, Boston, Massachusetts, United States

Abstract. Oxygen saturation (sO_2) of red blood cells (RBCs) in capillaries can indirectly assess local tissue oxygenation and metabolic function. For example, the altered retinal oxygenation in diabetic retinopathy and local hypoxia during tumor development in cancer are reflected by abnormal sO_2 of local capillary networks. However, it is far from clear whether accurate label-free optical oximetry (i.e., measuring hemoglobin sO_2) is feasible from dispersed RBCs at the single capillary level. The sO_2-dependent hemoglobin absorption contrast present in optical scattering signal is complicated by geometry-dependent scattering from RBCs. We present a numerical study of backscattering spectra from single RBCs based on the first-order Born approximation, considering practical factors: RBC orientations, size variation, and deformations. We show that the oscillatory spectral behavior of RBC geometries is smoothed by variations in cell size and orientation, resulting in clear sO_2-dependent spectral contrast. In addition, this spectral contrast persists with different mean cellular hemoglobin content and different deformations of RBCs. This study shows for the first time the feasibility of, and provides a theoretical model for, label-free optical oximetry at the single capillary level using backscattering-based imaging modalities, challenging the popular view that such measurements are impossible at the single capillary level. © *2017 Society of Photo-Optical Instrumentation Engineers (SPIE)* [DOI: 10.1117/1.JBO.22.2.025002]

Keywords: optical oximetry; capillary level; red blood cells; backscattering spectra; theoretical model; optical coherence tomography.

Paper 160569R received Aug. 25, 2016; accepted for publication Jan. 9, 2017; published online Feb. 3, 2017.

1 Introduction

Capillary networks support the function of biological tissues by providing oxygen and nutrients and carrying away metabolic waste. In turn, metabolic demands from tissue can induce remodeling of the capillary network. Local oxygen levels play a critical role in mediating this capillary–tissue relationship; for example, the retinal neovascularization in diabetic retinopathy and angiogenesis during tumor development are induced by local hypoxia. In the local microenvironment, oxygen unloads from hemoglobin and diffuses freely from red blood cells (RBCs) to tissues following the gradient of oxygen partial pressure (pO_2). Within capillaries, pO_2 determines the oxygen saturation (sO_2) of RBC hemoglobin. Thus, a measurement of capillary sO_2 can indirectly assess local tissue oxygenation and metabolic function. Because of its critical importance, several noninvasive and label-free methods have been designed to image microvascular networks in various tissue sites, such as optical coherence tomography (OCT) angiography,[1–5] adaptive optics laser scanning ophthalmoscopy (AOLSO),[6–9] laser speckle angiography,[10–13] and single RBC photoacoustic (PA) flowoxigraphy (FOG).[14] In addition, OCT and AOLSO have been used to image capillaries, and PA-FOG has been used to image capillary sO_2. However, an all-optical oximetry to measure sO_2 in capillaries has not yet been demonstrated due to the complications imposed by the discrete nature of cellular flow through a capillary. It has thus far been unclear whether accurate label-free optical oximetry to measure blood sO_2 is feasible at the capillary level.

The fundamental contrast in essentially all label-free optical oximetry arises from the distinct optical absorption spectra of oxygenated hemoglobin (HbO_2) and deoxygenated hemoglobin (Hb). Hemoglobin fills RBCs, with cell geometry creating a refractive index discontinuity between plasma and hemoglobin that scatters light. This light scattering is both geometry dependent and optical absorption dependent based on the Kramers–Kronig relations.[15] Although this mechanism is well characterized and understood for whole blood, it is far from clear at the capillary level where RBCs pass through in single file.[15] The scattering spectrum from a single RBC is highly dependent upon its geometry, orientation, and size. Therefore, it is challenging to optically measure sO_2 accurately at the capillary level without knowing the effects of geometry, orientation, and size on RBC scattering.[16]

To the best of our knowledge, for the first time, we demonstrate the feasibility of label-free optical oximetry from backscattered light of RBCs, considering cell geometry, orientation, and size variation. We focus on backscattered light since most *in vivo* optical imaging modalities use epi-illumination and detect signals in the backward direction. To calculate backscattering spectra of RBCs, we applied the first-order Born

approximation[17] for its simple analytical form and freedom in implementing arbitrary geometries. There are other reported numerical models simulating RBC optical properties, such as T-matrix and finite difference time domain,[18,19] but these are limited in fidelity of cellular geometry and computational efficiency when averaging over many RBC orientations. To validate our approach, we compared the first-order Born approximation with Mie theory for a large soft sphere similar to an RBC. We further verified our model experimentally from oxygenated and deoxygenated RBCs using visible light optical coherence tomography (vis-OCT).[3] We conclude that the oxygen-dependent absorption contrast of hemoglobin is present when averaging RBC backscattering spectra over cell orientation and size, and this contrast does not vary appreciably either when the mean cellular hemoglobin content (MCHC) varies or when the cells are deformed. This is promising for performing *in vivo* capillary-level backscattering-based optical oximetry using vis-OCT to measure local capillary sO_2 for early diagnosis, progression monitoring, and treatment evaluation of cancer and especially diabetic retinopathy. Currently, there has been no technique to measure retinal capillary sO_2, and OCT has been the standard of care in ophthalmology.

2 Theory

2.1 Theoretical Model for Capillary-Level Optical Oximetry

The RBC, or discocyte, is a biconcave disc-shaped cell containing hemoglobin. The complex refractive index of hemoglobin, $n = n' + in''$, is sO_2 dependent, as is the light scattering created by RBC geometry.[15] To quantitatively investigate RBCs' backscattering spectra, we consider a light wave with unit amplitude propagating in direction $\mathbf{s}_0$ that encounters an RBC in plasma. For any far-field point $\mathbf{r}$, the scattering process generates a spherical wave $E_s(\mathbf{r})$ propagating in direction $\mathbf{s} = \mathbf{r}/r$, where $r = |\mathbf{r}|$. This can be written as follows:

$$E_s(\mathbf{r}) = \mathbf{f}(\mathbf{s}, \mathbf{s}_0)\frac{e^{ikr}}{r}, \tag{1}$$

where $\mathbf{f}(\mathbf{s}, \mathbf{s}_0)$ is the scattering amplitude. For simplicity, we assume RBCs in plasma are far enough away from each other to scatter independently and apply the first-order Born approximation under which the field inside an RBC is approximated as the same as the incident field. Then

$$\mathbf{f}(\mathbf{s}, \mathbf{s}_0) = -\frac{k^2}{4\pi}\mathbf{s} \times [\mathbf{s} \times \mathbf{e}^{(i)}] \int_V [n_1^2(\mathbf{r}') - 1]e^{-ik(\mathbf{s}-\mathbf{s}_0)\cdot\mathbf{r}'}d\mathbf{r}', \tag{2}$$

where k is the wave number in the RBC, $n_1 = n/n_0$ is the relative refractive index within a scattering region of volume V, $E(\mathbf{r}') = \mathbf{e}^{(i)}e^{ik\mathbf{s}_0\cdot\mathbf{r}'}$ is the incident field (assumed as a plane wave), and $\mathbf{e}^{(i)}$ is the unit vector in the polarization direction of the incident field.

The differential scattering cross section is defined as

$$\sigma_s(\mathbf{s}, \mathbf{s}_0) = |\mathbf{f}(\mathbf{s}, \mathbf{s}_0)|^2. \tag{3}$$

We use $\sigma_s(-\mathbf{s}_0, \mathbf{s}_0)$ to present RBC backscattering spectrum, and $|\mathbf{s} \times (\mathbf{s} \times \mathbf{e}^{(i)})||_{\mathbf{s}=-\mathbf{s}_0} = 1$. Additionally, we assume RBCs as homogenous within their boundaries, thus

$$\sigma_s(-\mathbf{s}_0, \mathbf{s}_0) = |\mathbf{f}(-\mathbf{s}_0, \mathbf{s}_0)|^2 = |\eta\mathcal{F}\{R(\mathbf{r})\}_{\mathbf{k}_s=-2k\mathbf{s}_0}|^2, \tag{4}$$

where $\eta = \frac{k^2}{4\pi}(n_1^2 - 1)$, $R(\mathbf{r})$ is the RBC geometric function, and $\mathcal{F}$ represents the Fourier transform.

Equation (4) gives the backscattering spectrum of one single cell with a fixed orientation. We assume RBCs have random orientations in blood, thus the backscattering spectrum of one randomly oriented cell is given by averaging $\sigma_s(-\mathbf{s}_0, \mathbf{s}_0)$ over uniformly distributed incident directions

$$\sigma_b = \frac{1}{2\pi^2}\int_0^{2\pi}\int_0^{\pi}\sigma_s(-\mathbf{s}_0, \mathbf{s}_0)d\alpha\,d\beta, \tag{5}$$

where α is the polar angle, β is the azimuthal angle, and $\mathbf{s}_0 = (\cos\beta\sin\alpha, \sin\beta\sin\alpha, \cos\alpha)$. Here, $\mathbf{s}_0$ is varied to cover all cell orientations, and the trace of $\mathcal{F}\{R(\mathbf{r})\}_{\mathbf{k}_s}$ is a sphere with a radius of $2k$, illustrated in Fig. 1.

To characterize the intrinsic size variation of RBCs, we measured RBC sizes *in vitro* from anticoagulated bovine blood. The RBCs were sphered isovolumetrically with 0.03% sodium dodecyl sulfate (SDS) in phosphate buffered saline (PBS) and pipetted onto a glass slide.[20] The radius of spherical RBCs was quantified from two-dimensional (2-D) bright-field microscopic images (Leica, 40×). The detailed sample preparation is described in Sec. 3.2. A microscopic image of spherical RBCs is shown as the inset in Fig. 2. The radius of spherical bovine RBCs roughly followed a Gaussian distribution, with a mean of 2.63 μm, and a coefficient of variation (CV) of 5.54%. The CV is defined as the standard deviation divided by the mean value. The radius of spherical human RBCs measured by the same method also roughly followed a Gaussian distribution with a mean of 3.03 μm and a CV of 5.26%, shown in
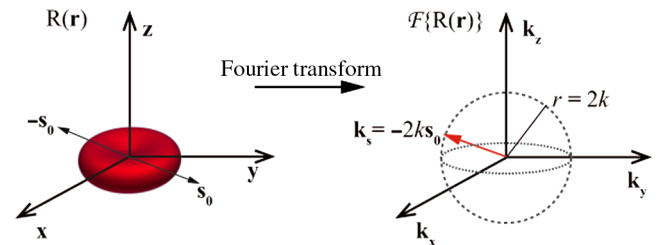

Fig. 1 Calculation of $\mathcal{F}\{R(\mathbf{r})\}$ for a single RBC.
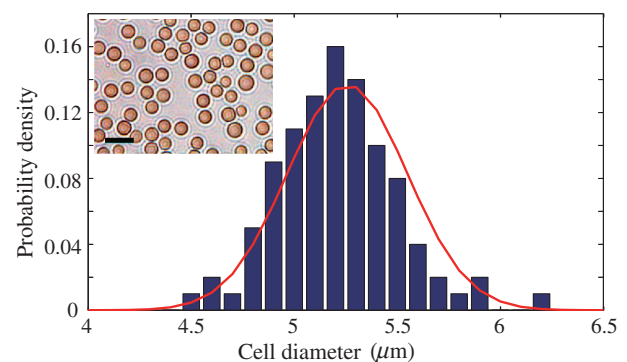

Fig. 2 The radius distribution of spherical bovine RBCs. Blue bars: the probability mass function of cell radius. The curve: Gaussian distribution (mean: 2.63 μm and CV: 5.54%). Spherical RBCs were made by adding 0.03% SDS to blood (ratio: 3:1). Inset panel: A microscopic image of spherical RBCs. Scale bar: 10 μm.

Appendix Fig. 9. As the sphering of RBCs was isovolumetric, we approximate the size (or volume) distribution of normal RBCs as that of the spherical RBCs characterized by microscope.

Considering the cell size, the RBC backscattering spectrum is given by averaging σ_b over size

$$\bar{\sigma}_b = \int_0^\infty \sigma_b(l) dP_l, \tag{6}$$

where l is the RBC long axis length and $dP_l \approx \frac{1}{\sqrt{2\pi\sigma^2}} e^{-\frac{(l-l_0)^2}{2\sigma^2}} dl$, with l_0 and σ denoting the mean and variance, respectively.

2.2 Geometric Model of Red Blood Cells

The geometric function for normal disk-shaped RBCs, or discocytes, is based on the Jacobi elliptic functions.[21] To account for deformations of RBCs in circulation and particularly in capillaries, parameters in the geometric function of a discocytes were modified to obtain six types of deformed RBCs, including stomatocyte I, stomatocyte II, stomatocyte III, and sphero-stomatocyte in the bloodstream, and bullet type and parachute type in capillaries.[21] The geometries of RBCs are inputs for simulations of the theoretical model.

2.3 Refractive Indices of Red Blood Cells and Plasma

We used complex refractive indices of RBCs, oxygenated and deoxygenated, in our simulations. We assume RBCs are internally homogeneous filled with hemoglobin solution. Using Kramers–Kronig relations, we generated the complex refractive index of RBCs according to the absorption coefficient of hemoglobin, which is calculated from the tabulated molar extinction coefficient for hemoglobin in water.[22] Since RBC hemoglobin content is usually between 300 and 360 g/L, we used 330 g/L in calculation of RBC refractive indices.[23] The refractive index of plasma we used is 1.35.[24]

3 Methods and Materials

3.1 Visible Light Optical Coherence Tomography System

We used spectral domain vis-OCT, an optical technique that probes tissue structure with backscattered light, to experimentally validate our model for discocytes. Spectroscopic analysis with vis-OCT can provide spatially resolved spectral information, allowing extraction of backscattering spectra from individual RBCs. The homebuilt vis-OCT used in this study incorporates a super-continuum laser for broadband illumination and a spectrometer covering a wavelength range from 520 to 630 nm. The transverse and axial resolutions of the vis-OCT system are 15 and 1.7 μm, respectively. A detailed description of the vis-OCT system is given in Ref. 3.

For RBC measurements, the following scanning protocol was used. In the fast scanning axis, each B-scan images consisted of 512 A-lines, covering a 0.55-mm length. In the slow scanning axis, 512 B-scans were required to cover a 0.55-mm range. The laser spot is translated along the fast scanning axis, whereas A-lines are acquired at a rate of 50 kHz, scanning back and forth between adjacent B-scans, so the total time to finish one vis-OCT scan is approximately 5.24 s. Although

the transverse resolution is not high enough to resolve fine features of a single RBC with a typical long axis length of around 8 μm, we were able to identify and extract spectrum from individual RBCs. This is possibly for two reasons. First, in our experiments, the RBCs are sparsely suspended. According to the detection volume ($0.55 \times 0.55 \times 3.02$ mm³), sample concentration (1%), hematocrit (0.4), and the size of RBCs characterized by microscope, the average distance between two RBCs in the sample is approximately 26.7 μm, which is much larger than the imaging resolution. Second, our scanning protocol oversampled in the transverse direction, making the distance between adjacent scan planes 1.07 μm to ensure sampling density was sufficient to distinguish the individual RBCs. Thus, we can still differentiate individual RBCs by vis-OCT in Fig. 4(b). Furthermore, for *in vivo* cases, where RBCs are closer to each other, the backscattering spectra measured by vis-OCT are averaged over many individual RBCs.

3.2 Sample Preparation

A sample of spherical RBC was prepared for measurements of cell size distribution. The sample was made by first adding 0.03% SDS PBS solution to bovine blood (Quad Five) at a volume ratio of 3:1. Then this mixture was diluted to a final concentration of 1% (bovine blood accounting for 1% of the whole sample volume) by adding more PBS. A drop of the sample was put on a glass slide and then imaged with a bright-field microscope (Leica, 40×). The radius of spherical RBCs was quantified from 2-D microscopic images.

Oxygenated and deoxygenated RBC samples were contained in glass petri dishes for vis-OCT measurements of backscattering spectra. Each glass petri dish contained approximately 10 mL of sample solution. For oxygenated samples, bovine blood was exposed to air for 1 h before dilution to 1% in PBS. For deoxygenated samples, 10% sodium dithionite ($Na_2S_2O_4$) in PBS was added to bovine blood at a ratio of 3:1 before the blood was diluted to 1% in PBS. To ensure samples were fully oxygenated or deoxygenated, a commercial oxygen probe (MI-730, Microelectrodes, Inc.) was used to measure the pO_2 independently.[25] To disperse RBCs in suspension, each sample was fully shaken before measurements were taken. For deoxygenated samples, each measurement was taken within 10 min of preparation with $Na_2S_2O_4$ to avoid oxygenation from air exposure.

3.3 Data Processing

RBC backscattering spectra were obtained by an inverse Fourier transform-short time Fourier transform method.[26] For each blood sample, seven independent vis-OCT scans ($0.55 \times 0.55 \times 3.02$ mm³) were acquired. In each vis-OCT scan, a threshold-based algorithm was used to segment regions containing RBCs, and spectra from all these regions were averaged to extract a mean spectrum. Afterward, each mean spectrum was normalized by its maximum value and seven independent mean spectra from the same sample were further averaged to produce a final spectrum with a standard deviation.

4 Results

4.1 Model Validation by Mie Theory

We first tested the validity of the first-order Born approximation used in this model derivation. We compared the backscattering

spectra calculated by our model and Mie theory of a single homogenous sphere with weak refractive index contrast to the background. The radius of the sphere was 2.25 μm, comparable to an RBC in size. The refractive indices of the sphere and background were 1.391 and 1.35, respectively, close to those of RBCs and plasma. In Fig. 3(a), the geometry-dependent backscattering spectra calculated by both methods exhibit similar oscillatory characteristics, caused by the interference of light reflected from the top and bottom boundaries of a single sphere. This similarity validates the first-order Born approximation for calculation of backscattering spectra of large soft spheres similar to RBCs. We then applied the complex refractive index of HbO$_2$ and Hb to spheres with the same radius to calculate their backscattering spectra by our model and Mie theory. The similar oscillatory character shown in Appendix Fig. 10 still dominates the backscattering spectra, making hemoglobin absorption contrast difficult to discern. However, when we averaged the spectra over size following a Gaussian distribution (mean: 2.25 μm; CV: 6%), the geometry-dependent spectra were smoothed out and the absorption contrast clearly emerged. To confirm this contrast, we also calculated the spectra by Mie theory for comparison. Results by both methods display similar hemoglobin absorption contrast in Fig. 3(b), confirming the feasibility of our model and indicating the possibility for deriving absorption-dependent sO$_2$ from backscattering at the cellular level.

4.2 Model Verification by Visible Light Optical Coherence Tomography

Our model was used to simulate the backscattering spectra of discocytes with different oxygenations. We then used vis-OCT to experimentally validate our model for discocytes by measuring the backscattering spectra of the prepared oxygenated and deoxygenated blood samples. The 2-D cross section and three-dimensional (3-D) configuration of a discocyte are shown in Fig. 4(a). The discocytes were assumed to have the same mean volume as the RBCs sphered by SDS, so their sizes also roughly followed a Gaussian distribution (mean long axis length: 7.5 μm; CV: 6%). The simulation results of oxygenated and deoxygenated RBCs are shown in Figs. 4(c)–4(d), indicating similar contrast to that of hemoglobin absorption. To verify sample oxygenation, a commercial oxygen probe was used to measure the pO$_2$ of the oxygenated and deoxygenated blood samples, which were 147.16 ± 5.04 mm Hg and

Fig. 4 (a) The geometry of a discocyte. (b) A pseudocolor B-scan image of RBCs in PBS by vis-OCT. Horizontal and vertical scale bars: 100 μm. Normalized backscattering spectra of (c) oxygenated and (d) deoxygenated discocytes from vis-OCT and our model (mean long axis length: 7.5 μm, CV: 6%), and equal-volumed spheres by Mie theory (mean radius: 2.625 μm, CV: 6%).

0.342 ± 0.129 mm Hg, corresponding to sO$_2$ values of $98.87 \pm 0.35\%$ and approximately 0%, respectively. A vis-OCT B-scan image of suspended RBCs is shown in Fig. 4(b). The spectra of oxygenated and deoxygenated RBCs with standard deviations are shown in Figs. 4(c)–4(d). In each vis-OCT scan, between 1000 and 2000 RBCs were segmented for averaging backscattering spectra. The backscattering spectra calculated by Mie theory for equal-volumed spherical RBCs are shown for comparison. All results are normalized by their maximum values, respectively.

The results of our model, Mie theory, and experiments show similar absorption contrast in Figs. 4(c)–4(d) without oscillations. Compared with Mie theory, results of our model are closer to experiments in magnitude, especially for the deoxygenated samples. Although results of Mie theory show greater contrast, especially for the oxygenated samples, they are not well within the margin of error of experiments. This suggests that a cell's geometry affects its backscattering spectrum, and our model can serve as a more accurate method to calculate backscattering spectra of nonspherical particles.
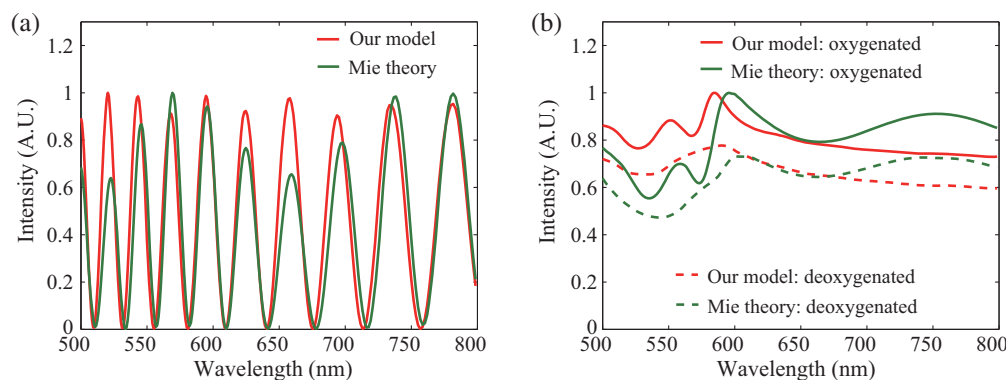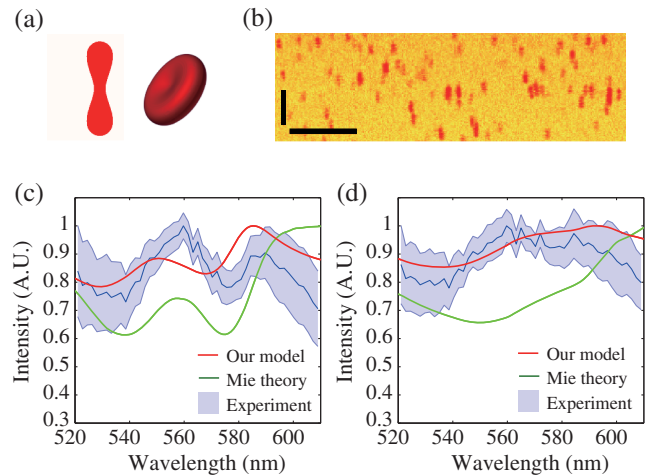

Fig. 3 Normalized backscattering spectra by Mie theory and our model for spheres: (a) Uniform radius: 2.25 μm; refractive index: 1.391; (b) mean radius: 2.25 μm; CV: 6%; refractive index: complex refractive index of HbO$_2$ and Hb. Refractive index of background: 1.35.

4.3 Model Simulations of Red Blood Cells with Different Mean Cellular Hemoglobin Contents

We calculated refractive indices of RBCs for simulations based on constant MCHC of 330 g/L, but practically this MCHC can vary between 300 and 360 g/L, resulting in variations of RBC refractive indices.[23] Thus, we explored how the variation in MCHC affects RBC backscattering spectra by setting the MCHC as 300, 320, 340, and 360 g/L, respectively. Under different MCHCs, the backscattering spectra of RBCs were calculated and averaged over orientation and size. The results are shown in Fig. 5. The oxygenation contrast in backscattering spectra of RBCs persists with different MCHCs, but higher MCHC tends to generate backscattering spectra with more intensive oxygenation contrast. This demonstrates the reasonability of using 330 g/L as MCHC to do all our simulations.
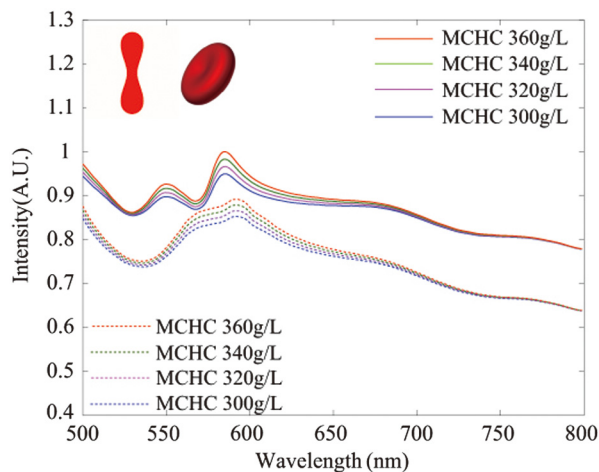
Fig. 5 The influence of MCHC on backscattering spectra of RBCs.

4.4 Model Simulations of Deformed Red Blood Cells

RBCs in circulation can deform by elastic and electrical forces, surface tension, and osmotic or hydrostatic pressures.[21] In particular, RBCs can deform as bullet-like or parachute-like shapes as they pass through capillaries.[27,28] To account for this, we explored the effect of cell deformations in capillaries on backscattering spectra. For comparison, four general RBC deformations in the bloodstream are also explored. Six RBC deformations, including bullet type ($l = 5.35~\mu m$, $h_+ = 4.125~\mu m$, $h_- = 1.375~\mu m$, $m_+ = 0.12$, and $m_- = 0.35$) and parachute type ($l = 5.525~\mu m$, $h_+ = 4.55~\mu m$, $h_- = 0.15~\mu m$, $m_+ = 0$, and $m_- = 0.99$) in capillaries, and stomatocyte type I ($l = 7.8~\mu m$), stomatocyte II ($l = 6.525~\mu m$), stomatocyte III ($l = 6.025~\mu m$), and sphero-stomatocyte ($l = 5.825~\mu m$) in the bloodstream,[21] which have the same mean volume, were inputs for model simulation. Their 2-D cross sections and 3-D configurations are on the top left of Figs. 6(a)–6(f). Sizes of all deformations followed a Gaussian distribution (CV: 6%). We compare their backscattering spectra in Figs. 6(a)–6(f), with all curves normalized by maximum values of the oxygenated RBCs, respectively. The contrasts are all similar, indicating that the backscattering spectra showing hemoglobin absorption contrast do not appreciably vary for differently deformed RBCs.

5 Discussion

The simulation results of RBC backscattering spectra are averaged over both cell orientations and size, but the variation in cell size is the key to reveal hemoglobin absorption contrast in RBC backscattering spectra. For a single RBC, interference of reflected light from its scattering interfaces leads to an oscillatory backscattering spectrum, which is dependent upon the cell's effective thickness and the illumination wavelength. This effective thickness has an intimate dependence on RBC orientation and size. A single RBC of three different orientations
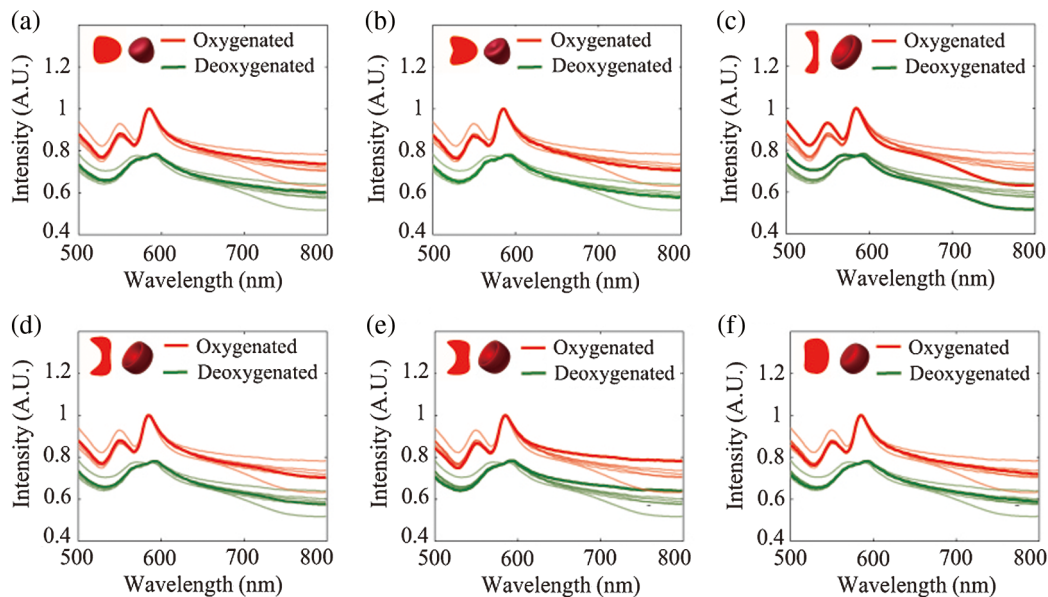
Fig. 6 The geometries of deformed RBCs and their backscattering spectra calculated by our model: (a) bullet type, (b) parachute type, (c) stomatocyte type I, (d) stomatocyte type II, (e) stomatocyte type III, and (f) sphero-stomatocyte. In each case, only the curves for the geometry on the top left are highlighted, whereas the others are semitransparent.

with respect to incident light has different backscattering spectra, shown in Figs. 7(a)–7(c). When we take the ensemble average of RBC thicknesses over all incident directions, the oscillatory backscattering spectra still overwhelm the oxygenation spectral contrast, shown in Fig. 7(d). However, when we further average the spectra over Gaussian-distributed cell sizes with a CV large enough, the oscillatory spectra from each single size are smoothed. This smoothing reveals underlying absorption profiles as the oscillations average out, leaving the distinct sO_2-dependent contrast. The effect of CV on backscattering spectra of spherical RBCs by Mie theory is shown in Appendix Fig. 11.

The capillary sO_2 can be quantified from contrast in the RBC backscattering spectra averaged over cell orientation and size, but it is impossible to measure a single RBC's oxygenation through its optical backscattering spectrum due to its high sensitivity to cellular orientation. Realistically, for future *in vivo* capillary measurements, the RBC backscattering spectra measured with vis-OCT will be averaged over time for a given location and/or over a given region containing capillary networks to obtain a confident measurement of averaged sO_2. Furthermore, sO_2 quantified in this manner is more reliable to assess local tissue oxygenation than the sO_2 of individual RBCs. For example, the local hypoxia in diabetic retinopathy and cancer are reflected by the sO_2 of a local capillary network, instead of the sO_2 of any single RBC passing through a capillary. For the necessary number of RBCs averaged to show the oxygenation contrast in backscattering spectra, we segmented between 1000 and 2000 RBCs for each vis-OCT scan. The minimum number of RBCs that need to be averaged to see oxygenation contrast is 147 ± 3, assuming a *p* value of 0.05 for discrimination of differing spectral features between oxygenated and deoxygenated RBCs. To guarantee sufficient RBCs are averaged in future *in vivo* capillary measurements, one could repeatedly scan capillary cross sections or scan a small region containing a bed of capillaries with a sufficient number of blood cells to average. Assuming the capillary flow velocity as 0.65 mm/s,[29]
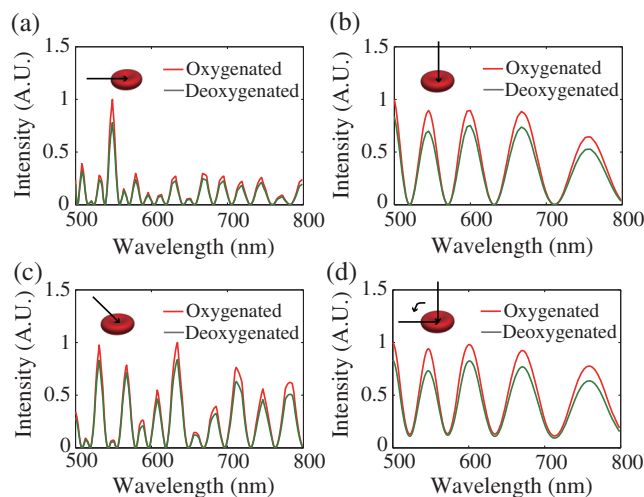

Fig. 7 The backscattering spectra of an oxygenated or deoxygenated RBC with different incident directions of light. The incident direction of light is parallel to the disk plane of cell in (a), perpendicular to the disk plane of the cell in (b), and 45 deg to the disk plane of cell in (c). The RBC backscattering spectra in (d) are averaged over all incident directions. [RBC long axis length in (a)–(c): 7.5 μm; RBC long axis length in (d): 7.5 μm].
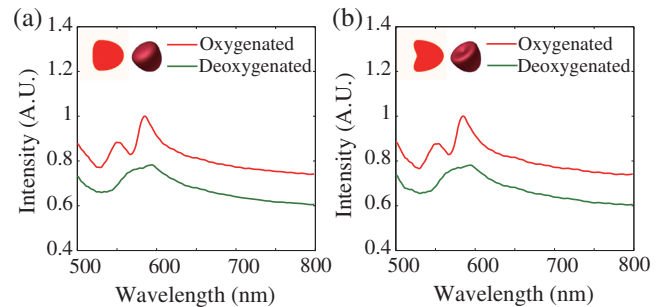

Fig. 8 The 2-D cross sections and 3-D configurations of deformed RBCs in capillaries and their backscattering spectra by our model: (a) bullet type and (b) parachute type. The backscattering spectra are averaged over similar cell orientations ($+/-\pi/18$) and Gaussian-distributed cell sizes (CV: 6%).

capillary density as 112 capillaries/mm^2,[30] the RBC size as 8 μm, blood hematocrit as 0.4, and 512 A-lines in each B-scan for a range of 0.55 mm, acquiring 147 RBCs in a 1-mm-thick skin layer would take 38 s of continuous acquisition time, or alternatively scanning a total skin volume of $0.16 \times 0.16 \times 1$ mm^3. Such a method would be experimentally feasible for *in vivo* applications.

Physiologically, RBC orientations in capillaries depend on the flow direction, so we explored how cell orientation affects its backscattering spectra in capillaries and found that the cell orientation in capillaries has little influence on revealing hemoglobin oxygenation contrast in backscattering spectra. In this case, we assume the capillary flow direction to be perpendicular to the incident light, and most cell orientations to be axisymmetric about this flow direction ($\pm\pi/18$). This is the most common backscattering-based imaging orientation. Cell sizes are also Gaussian distributed (CV: 6%). The resulting backscattering spectra of bullet- and parachute-type RBCs in Fig. 8 still show similar contrast, indicating little influence of cell orientations on backscattering spectra in capillaries. Actually, due to capillary orientation and elasticity, interactions of RBCs with other blood cells, etc., the distribution of RBC orientations in capillaries is difficult to predict.[31,32] Without explicitly knowing the orientation, a more relaxed condition (uniformly distributed cell orientations) is intuitively feasible.

Discrepancies between vis-OCT measurements and our model for discocytes can be attributed to true cell geometries deviating from our geometric model and the exclusion of higher-order scattering in the first-order Born approximation. However, our method requires acquisition of signals from RBCs over time for a given location and/or over a given region containing capillary networks to allow an ensemble average over different orientations and sizes, which is inevitable as RBCs travel through the capillary. Therefore, our results demonstrate the feasibility of optical oximetry based on backscattered light at the capillary level. For future *in vivo* measurements by vis-OCT, we can obtain two calibration curves, the backscattering spectra of oxygenated and deoxygenated RBCs by vis-OCT and quantify the sO_2 of experimental backscattering spectra according to calibration curves through least-square fitting.

6 Conclusion

To summarize, we provide a theoretical model for backscattering-based oximetry at the single capillary level, which has not
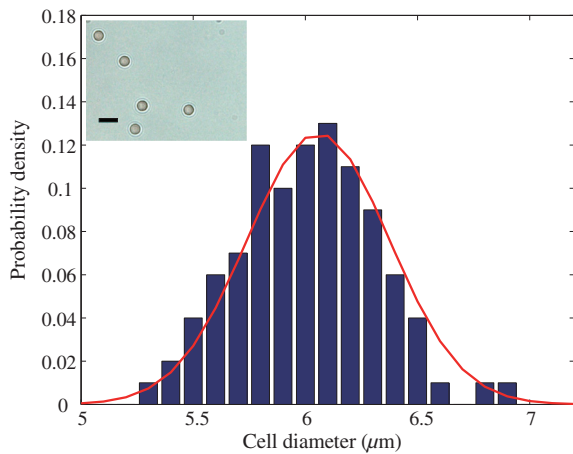
Fig. 9 The radius distribution of spherical human RBCs. Blue bars: the probability mass function of cell radius. The curve: Gaussian distribution with a mean of 3.03 μm and a CV of 5.26%. Spherical RBCs were made by adding 0.03% SDS (in PBS) to blood at a ratio of 3:1. Inset panel: a microscopic image of spherical RBCs. Scale bar: 10 μm.
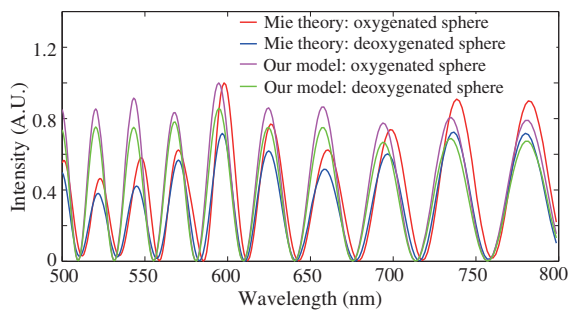

Fig. 10 Comparison of normalized backscattering spectra calculated by Mie theory and our model for spheres (spherical RBCs) with a uniform radius of 2.25 μm. Refractive index of spheres: complex refractive index of HbO_2 and Hb. Refractive index of background: 1.35.

previously been explored theoretically. This model was verified by Mie theory and experiments using vis-OCT. The backscattering spectra calculated by this model show clear hemoglobin absorption contrast when considering variations in cell orientation and size, allowing the sO_2 of RBCs to be characterized. This is promising for *in vivo* backscattering-based optical oximetry at the single capillary level to measure local capillary sO_2 for early diagnosis, progression monitoring, and treatment evaluation of diabetic retinopathy and cancer.

Disclosures

All authors declare that there are no other relevant conflicts of interests in this paper.

Appendix

Figures 9–11 are supplementary figures.

References

1. J. Yi et al., "Visible-light optical coherence tomography for retinal oximetry," *Opt. Lett.* **38**(11), 1796–1798 (2013).
2. J. Yi et al., "In vivo functional microangiography by visible-light optical coherence tomography," *Biomed. Opt. Express* **5**(10), 3603–3612 (2014).
3. S. Chen, J. Yi, and H. F. Zhang, "Measuring oxygen saturation in retinal and choroidal circulations in rats using visible light optical coherence tomography angiography," *Biomed. Opt. Express* **6**(8), 2840–2853 (2015).
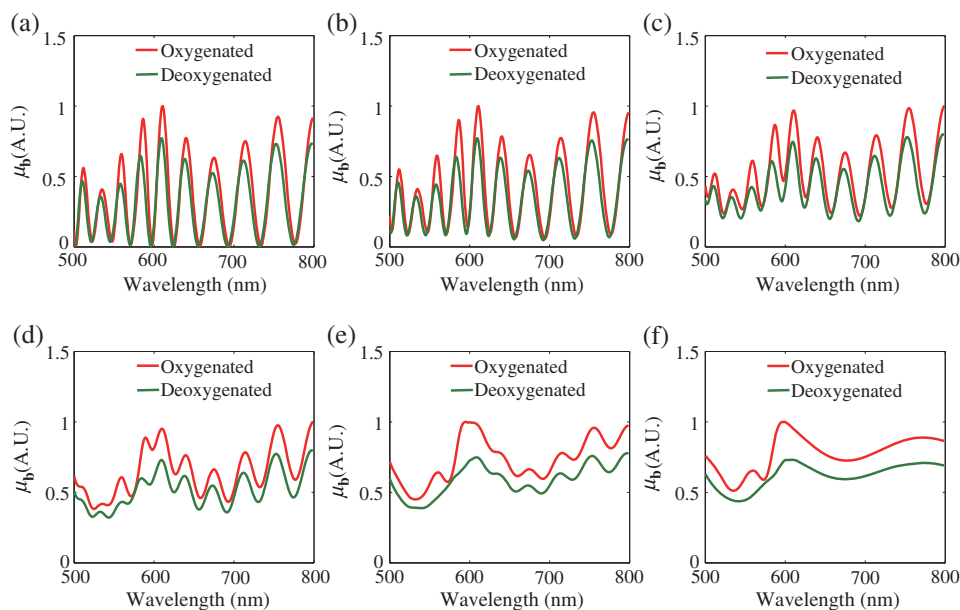

Fig. 11 The effect of CV on backscattering spectra of spherical oxygenated and deoxygenated RBCs with a mean radius of 2.3 μm by Mie theory. CV: (a) 0.1%, (b) 0.5%, (c) 1%, (d) 1.5%, (e) 2%, and (f) 5%.

4. S. P. Chong et al., "Quantitative microvascular hemoglobin mapping using visible light spectroscopic optical coherence tomography," *Biomed. Opt. Express* **6**(4), 1429–1450 (2015).

5. L. Kagemann et al., "Spectral oximetry assessed with high-speed ultra-high-resolution optical coherence tomography," *J. Biomed. Opt.* **12**(4), 041212 (2007).

6. R. D. Ferguson et al., "Adaptive optics scanning laser ophthalmoscope with integrated wide-field retinal imaging and tracking," *J. Opt. Soc. Am. A* **27**(11), A265–A277 (2010).

7. A. Pinhas et al., "In vivo imaging of human retinal microvasculature using adaptive optics scanning light ophthalmoscope fluorescein angiography," *Biomed. Opt. Express* **4**(8), 1305–1317 (2013).

8. R. J. Zawadzki et al., "Integrated adaptive optics optical coherence tomography and adaptive optics scanning laser ophthalmoscope system for simultaneous cellular resolution in vivo retinal imaging," *Biomed. Opt. Express* **2**(6), 1674–1686 (2011).

9. T. Y. Chui, D. A. VanNasdale, and S. A. Burns, "The use of forward scatter to improve retinal vascular imaging with an adaptive optics scanning laser ophthalmoscope," *Biomed. Opt. Express* **3**(10), 2537–2549 (2012).

10. K. Murari et al., "Contrast-enhanced imaging of cerebral vasculature with laser speckle," *Appl. Opt.* **46**(22), 5340–5346 (2007).

11. G. Watanabe, H. Fujii, and S. Kishi, "Imaging of choroidal hemodynamics in eyes with polypoidal choroidal vasculopathy using laser speckle phenomenon," *Jpn. J. Ophthalmol.* **52**(3), 175–181 (2008).

12. A. Rege et al., "In vivo laser speckle imaging reveals microvascular remodeling and hemodynamic changes during wound healing angiogenesis," *Angiogenesis* **15**(1), 87–98 (2012).

13. G. Mahé et al., "Assessment of skin microvascular function and dysfunction with laser speckle contrast imaging," *Circulation* **5**(1), 155–163 (2012).

14. L. Wang, K. Maslov, and L. V. Wang, "Single-cell label-free photoacoustic flowoxigraphy in vivo," *Proc. Natl. Acad. Sci. U. S. A.* **110**(15), 5759–5764 (2013).

15. D. J. Faber et al., "Oxygen saturation-dependent absorption and scattering of blood," *Phys. Rev. Lett.* **93**(2), 028102 (2004).

16. M. Kinnunen et al., "Effect of the size and shape of a red blood cell on elastic light scattering properties at the single-cell level," *Biomed. Opt. Express* **2**(7), 1803–1814 (2011).

17. J. Lim et al., "Born approximation model for light scattering by red blood cells," *Biomed. Opt. Express* **2**(10), 2784–2791 (2011).

18. A. M. Nilsson et al., "T-matrix computations of light scattering by red blood cells," *Appl. Opt.* **37**(13), 2735–2748 (1998).

19. J. Q. Lu, P. Yang, and X.-H. Hu, "Simulations of light scattering from a biconcave red blood cell using the finite-difference time-domain method," *J. Biomed. Opt.* **10**(2), 024022 (2005).

20. Y. R. Kim and L. Ornstein, "Isovolumetric sphering of erythrocytes for more accurate and precise cell volume measurement by flow cytometry," *Cytometry* **3**(6), 419–427 (1983).

21. S. Muñoz et al., "Elastic energy of the discocyte–stomatocyte transformation," *Biochim. Biophys. Acta* **1838**(3), 950–956 (2014).

22. S. Prahl et al., "Optical absorption of hemoglobin," *Oregon Medical Laser Center*, http://omlc.ogi.edu/spectra/hemoglobin/index.html (1999).

23. M. Friebel and M. Meinke, "Model function to calculate the refractive index of native hemoglobin in the wavelength range of 250-1100 nm dependent on concentration," *Appl. Opt.* **45**(12), 2838–2842 (2006).

24. A. G. Borovoi, E. I. Naats, and U. G. Oppel, "Scattering of light by a red blood cell," *J. Biomed. Opt.* **3**(3), 364–372 (1998).

25. G. R. Kelman, "Digital computer subroutine for the conversion of oxygen tension into saturation," *J. Appl. Physiol.* **21**(4), 1375–1376 (1966).

26. J. Yi, J. Gong, and X. Li, "Analyzing absorption and scattering spectra of micro-scale structures with spectroscopic optical coherence tomography," *Opt. Express* **17**(15), 13157–13167 (2009).

27. G. Tomaiuolo et al., "Red blood cell deformation in microconfined flow," *Soft Matter* **5**(19), 3736–3740 (2009).

28. G. Coupier et al., "Shape diagram of vesicles in Poiseuille flow," *Phys. Rev. Lett.* **108**(17), 178106 (2012).

29. B. Fagrell, A. Fronek, and M. Intaglietta, "A microscope-television system for studying flow velocity in human skin capillaries," *Am. J. Physiol.-Heart Circulatory Physiol.* **233**(2), H318–H321 (1977).

30. A. Jaap et al., "Skin capillary density in subjects with impaired glucose tolerance and patients with type 2 diabetes," *Diabetic Med.* **13**(2), 160–164 (1996).

31. J. H. Jeong et al., "Measurement of RBC deformation and velocity in capillaries in vivo," *Microvasc. Res.* **71**(3), 212–217 (2006).

32. A. Mishra et al., "Imaging pericytes and capillary diameter in brain slices and isolated retinae," *Nat. Protoc.* **9**(2), 323–336 (2014).

Biographies for the authors are not available.